Semiclassical trace formula for truncated spherical well potentials: Toward the analyses of shell structures in nuclear fission processes

Ken-ichiro Arita

Department of Physics, Nagoya Institute of Technology, Nagoya 466-8555, Japan

Trace formulas for the contributions of degenerate periodic-orbit families to the semiclassical level density in truncated spherical hard-wall potentials are derived. In addition to the portion of the continuous periodic-orbit family contribution which persists after truncation, end-point corrections to the truncated family should be taken into account. I propose a formula to evaluate these end-point corrections as separate contributions of what I call marginal orbits. Applications to the two-dimensional billiard and three-dimensional cavity systems with the three-quadratic-surfaces shape parametrization, initiated to describe the nuclear fission processes, reveal unexpectedly large effects of the marginal orbits.

I. INTRODUCTION

In quantum many-body systems such as nuclei and microclusters, the fluctuations in the physical quantities like energy and deformations as functions of the constituent particle number are essentially governed by the single-particle shell effects. In many cases, gross structures in the single-particle energy spectra show regularly oscillating patterns. The origins of such patterns are clearly explained using the semiclassical periodic-orbit theory (POT), which expresses the quantum level density and also shell energy in terms of the contributions of classical periodic orbits. This formula, known as the trace formula, immediately after its discovery by Gutzwiller [1,2] and independently by Balian-Bloch [3,4] was recognized as being extremely useful in explaining the properties of gross shell structures in nuclei, shell and supershell structures in metallic clusters, and so on. Bunchings of levels in isotropic harmonic oscillator systems or in anisotropic ones with rational frequency ratios are related to the conditions for most of the classical orbits to be periodic with short periods, which qualitatively explain the origins of spherical and superdeformed shell structures [5]. Strutinsky and coworkers applied the trace formula to explain the deformed shell structures in the nuclear mean field [6,7]. Nishioka *et al.* have set out an elegant explanation of the supershell structures in metallic clusters as the interference of the contributions of triangle and square type periodic orbits in the spherical mean field potential [8].

In the low-energy fission of actinide nuclei, the double-humped structure in the fission barrier and the asymmetric fragment-mass distributions are caused by the quantum shell effect [9]. According to the POT, shell structures associated with the periodic orbits which oscillate twice along the minor axis while they oscillate once along the major axis in a strongly elongated mean-field potential play a significant role in building the double-humped fission barrier [10–12]. Brack *et al.* have made a semiclassical analysis of the origin of the asymmetric fission using a simple cavity potential model

[13]. They have found that the valleys in the potential energy surface from symmetric minima toward strongly elongated asymmetric shapes can be nicely explained by the contribution of the shortest periodic orbit.

More specifically, the fragment-mass distribution in low-energy nuclear fission experiments suggests strong effects of the fragment shell structures. In the fission of actinide nuclei, the mass numbers of the heavier fragments are around 140, independent of the mass of the parent nuclei, which is close to that of the doubly-magic ^{132}Sn ($Z = 50$, $N = 82$). On the other hand, the recent experiment on the fission of neutron-deficient mercury isotope ^{180}Hg shows asymmetric fragment-mass distribution in spite of the stability of the fragments ^{90}Zr ($Z = 40$, $N = 50$) in the case of symmetric fission [14]. According to the theoretical analysis of the five-dimensional potential energy surface with the macroscopic-microscopic model [15], the hindrance of symmetric fission in ^{180}Hg is successfully interpreted as the result of a large potential barrier along the symmetric path in the potential energy surface, which stems mainly from the shell effect. This implies the importance of the deformed shell effect in the fission process, rather than those of the final daughter nuclei, to understand the properties of the fragment-mass distributions.

For the nucleus in the fission process, a neck is formed in the mean-field potential, and it gradually separates the system into two nascent fragment parts. In the following, I use the term "prefragment" denoting the nascent fragment to distinguish it from those after the scission. When the neck is developed, one may expect a kind of shell effect which stabilize the shapes and sizes of the prefragment parts. An unexpectedly large prefragment shell effect at a rather early stage of the fission process, just after getting over the second saddle, was suggested by the two-center shell model calculation [16]. Emergence of the prefragments, which have density profiles similar to those of stable spherical magic nuclei, was found in modern microscopic density-functional calculations [17,18]. Although those results suggest the significance of

shell effects associated with the prefragments, it is not a simple problem to extract the effect of each prefragment exclusively out of the total shell effect in purely quantum mechanical approaches, because most of the single-particle wave functions are delocalized in the potential.

Here, let us take notice of the fact that the semiclassical level density is represented by sum of the contributions of classical periodic orbits. Formation of neck (constriction) in the potential yields periodic orbits which are confined in each of the prefragment parts, which will be briefly termed as "prefragment orbits" below. Then, one can define the prefragment shell effects unambiguously by the contributions of those prefragment orbits to the semiclassical level density. Note that those orbits bring about the same kinds of quantum fluctuation to the system as in the case where they exist in an isolated fragment. Taking account of those features, one can analyze the roles of the neck formation in stabilizing the shapes of nuclei in the fission processes.

In order to focus on the effect of shape evolution, a simple cavity potential model will be employed but with the ingenious three-quadratic-surfaces (TQS) shape parametrization, which is useful in describing the nuclear fission processes. In this parametrization, two prefragments and the neck part between them are represented by quadratic surfaces, and their shapes are easily controlled by the shape parameters. Supposing that the prefragment has a spherical shape, which provides the strongest shell effect, one must necessarily treat the classical periodic-orbit families confined in the truncated spheres for the semiclassical analysis of the deformed shell effect. Periodic orbits which form a continuous family having identical action and stability are called degenerate, and the order of degeneracy is defined by the number of independent continuous parameters for the family. The polygon and diameter orbits form three- and two-parameter families in the truncated spherical cavity, but the ranges of the parameters are restricted and their contributions to the semiclassical level density are suppressed compared with those in the nontruncated spherical cavity.

In this paper, I derive the contribution of degenerate periodic-orbit family confined in the truncated spherical cavity potential based on the Balian-Bloch formula [4]. For simplicity, I begin with a two-dimensional (2D) billiard system using the same shape parametrization. In Sec. II, the essence of the Balian-Bloch trace formula is briefly outlined, and then contributions of degenerate families of periodic orbits in 2D truncated circular billiard and a three-dimensional (3D) truncated spherical cavity are derived. As numerical applications, I examine the single-particle level densities in the TQS billiard and cavity models in Sec. III. Section IV is devoted to a summary and concluding remarks. Some details in derivations of the trace formulas are given in the Appendix.

II. TRACE FORMULA FOR DEGENERATE ORBITS IN HARD-WALL POTENTIALS

A. Balian-Bloch formula

I shall first outline the derivation of the Balian-Bloch formulas for semiclassical level density in hard-wall potential

models [3,4]. Consider a particle of mass M which moves freely inside the closed surface S and is reflected ideally on the wall. The energy of the particle is given by $E = \hbar^2 k^2 / 2M$ with the constant wave number k. The Green's function for such a system is defined by

$$\left(-\frac{\hbar^2}{2M}\nabla^2 - E\right)G(\boldsymbol{r}, \boldsymbol{r}'; E) = \delta(\boldsymbol{r} - \boldsymbol{r}'), \qquad (2.1)$$

with the Dirichlet boundary condition $G(\boldsymbol{r}_s, \boldsymbol{r}'; E) = 0$ for $\boldsymbol{r}_s$ on the wall S and $\boldsymbol{r}'$ inside the wall. In terms of the Green's function, level density $g(E)$ is expressed as

$$g(E) = \frac{1}{\pi}\operatorname{Im}\int_V d\boldsymbol{r}\, G(\boldsymbol{r}, \boldsymbol{r}; E + i0), \qquad (2.2)$$

where the volume integral is taken over the interior region V of the closed surface S. By introducing a double-layer potential on the surface to ensure the boundary condition [19], a multiple-reflection expansion formula for the Green's function is derived [3], which is expressed as

$$G(\boldsymbol{r}_0, \boldsymbol{r}_0'; E)$$

$$= G_0(0, 0') + \sum_{p=1}^{\infty}\left(\frac{\hbar^2}{M}\right)^p \oint_S dS_1 \cdots dS_p \frac{\partial G_0(0, p)}{\partial n_p}$$

$$\times \frac{\partial G_0(p, p-1)}{\partial n_{p-1}} \cdots \frac{\partial G_0(2, 1)}{\partial n_1} G_0(1, 0'). \qquad (2.3)$$

Here, $G_0(b, a) = G_0(\boldsymbol{r}_b, \boldsymbol{r}_a; E + i0)$ denotes the Green's function for a free particle, and $\partial/\partial n_a$ represents the component of the gradient normal to the surface S at $\boldsymbol{r}_a$. Each term on the right-hand side can be interpreted as the contribution of the wave, which starts off at $\boldsymbol{r}_0'$ and hits p times on the wall S at $\boldsymbol{r}_1, \ldots, \boldsymbol{r}_p$ before arriving at $\boldsymbol{r}_0$. Substituting (2.3) into (2.2), one has

$$g(E) = g_0(E) + \frac{1}{\pi}\operatorname{Im}\sum_{p=1}^{\infty}\left(\frac{\hbar^2}{M}\right)^p \int_V d\boldsymbol{r}_0 \oint_S dS_1 \cdots dS_p$$

$$\times \frac{\partial G_0(0, p)}{\partial n_p}\frac{\partial G_0(p, p-1)}{\partial n_{p-1}} \cdots \frac{\partial G_0(2, 1)}{\partial n_1} G_0(1, 0). \qquad (2.4)$$

For sufficiently large k, integrations on the right-hand side can be carried out using the stationary-phase approximation (SPA), and the level density is expressed as the sum over contributions of the stationary paths, namely, the classical periodic orbits. The free-particle Green's function G_0 is given by

$$\frac{\hbar^2}{2M}G_0(\boldsymbol{r}_b, \boldsymbol{r}_a; E) = \begin{cases} \frac{i}{4}H_0^{(1)}(kr_{ab}) \simeq \frac{e^{ikr_{ab}}}{\sqrt{8\pi kr_{ab}/i}} & \text{(2D)}, \\ \frac{e^{ikr_{ab}}}{4\pi r_{ab}} & \text{(3D)} \end{cases}$$

$$(2.5)$$

for the spatial dimensions 2 and 3, with $r_{ab} = |\boldsymbol{r}_b - \boldsymbol{r}_a|$. In the expression for 2D billiard, $H_\nu^{(1)}$ denotes the νth order Hankel function of the first kind, and the approximation on the right-hand side holds for the asymptotic limit $kr_{ab} \gg 1$. Using these expressions, one arrives at the general formula

for the semiclassical level density

$$g(E) = g_0(E) + \text{Re} \sum_\beta a_\beta(k) \oint dS_1 \cdots dS_{p_\beta} e^{ikl_\beta}. \quad (2.6)$$

l_β denotes the total length of the polygon orbit with $p = p_\beta (\geqslant 2)$ vertices on the wall S,

$$l_p = r_{12} + r_{23} + \cdots + r_{p-1,p} + r_{p1}, \quad (2.7)$$

which is expressed as a function of the local surface coordinates around the vertices of the stationary orbit β. The preexponential factor is evaluated for the stationary orbit β and is put out of the integral into $a_\beta(k)$ as usual in the SPA (see Ref. [4] for its explicit form in the 3D case). For a system with only isolated periodic orbits, all the surface integrals in (2.6) are carried out by expanding the length l_p with respect to the surface coordinates up to the second order around the stationary point, and the integrals are reduced to the Fresnel type. The result can be translated to the Gutzwiller trace formula [1,2]

$$g(E) = g_0(E) + \sum_\beta \sum_{m=1}^{\infty} \frac{T_\beta}{\pi \hbar \sqrt{\left| \det \left(\mathsf{M}_\beta^m - I \right) \right|}}$$
$$\times \cos \left(mkL_\beta - \frac{\pi}{2} \mu_{m\beta} \right). \quad (2.8)$$

On the right-hand side, the sum is taken over all the primitive periodic orbits β and the numbers of their repetitions m ($m = 1$ corresponds to the primitive orbit). T_β is the period of the primitive orbit β,

$$T_\beta = \frac{dS_\beta}{dE} = \frac{ML_\beta}{\hbar k}, \quad (2.9)$$

with the wave number $k = \sqrt{2ME}/\hbar$ and the orbit length L_β. In Eq. (2.8), M_β represents the monodromy matrix which describes the stability of the orbit, and $\mu_{m\beta}$ is the Maslov index related to the number of focal and caustic points along the orbit [1,2]. The level density in terms of the wave-number variable k is written as

$$g(k) = g(E) \frac{dE}{dk}$$
$$= g_0(k) + \sum_\beta \sum_{m=1}^{\infty} \frac{L_\beta}{\pi \sqrt{\left| \det \left(\mathsf{M}_\beta^m - I \right) \right|}}$$
$$\times \cos \left(mkL_\beta - \frac{\pi}{2} \mu_{m\beta} \right). \quad (2.10)$$

In a Hamiltonian system with continuous symmetries, generic periodic orbits form continuous families generated by the symmetry transformations. For such degenerate periodic orbits, some of the integrals in (2.6) should be carried out exactly with respect to the continuous parameters for the family. The extensions of the Gutzwiller trace formula to systems with continuous symmetries are presented in [6,20,21].

In a 2D circular billiard with radius R_0, there are regular polygon orbits labeled by the two integers (p, t), where p is the number of vertices and t is the number of turns around the center ($p \geqslant 2t$). A primitive orbit is specified by an

incommensurable pair of p and t, and the repeated orbit with repetition number m is denoted by $m(p, t)$. Each of those orbits forms a one-parameter family due to the rotational symmetry. Then, integrals in Eq. (2.6) are done for the one surface coordinate associated with the degeneracy exactly, and for the others using the SPA. The analytic expression of the result for the orbit (p, t) is obtained as [22,23]

$$g_{m(p,t)}^{(\text{circ})}(k) = 2R_0 \sqrt{kR_0} A_{m(p,t)}^{(\text{circ})} \sin \left(kmL_{pt} - \frac{\pi}{2} \mu_{m(p,t)}^{(\text{circ})} \right), \quad (2.11)$$

with the dimensionless energy-independent amplitude factor A, orbit length L, and the Maslov index μ given by

$$A_{m(p,t)}^{(\text{circ})} = w_{pt} \sqrt{\frac{\sin^3 \varphi_{pt}}{mp\pi}}, \quad \varphi_{pt} = \frac{\pi t}{p},$$
$$L_{pt} = 2pR_0 \sin \varphi_{pt}, \quad \mu_{m(p,t)}^{(\text{circ})} = 3mp - \frac{3}{2}. \quad (2.12)$$

Here, w_{pt} represents the time-reversal factor: It takes the value 2 for polygon orbits ($p > 2t$) to take into account the orbits turning clockwise and anticlockwise, while it takes the value 1 for diameter orbits ($p = 2t$) whose time reversals are equivalent to the original ones.

In a 3D spherical cavity potential with radius R_0, there exist the same set of periodic orbits as in the circular billiard but with different degeneracies [4]. Polygon orbits ($p > 2t$) form three-parameter families generated by the three-dimensional rotations. To obtain the contribution of such a family, the integrals in Eq. (2.6) are done for three surface coordinates associated with the degeneracy exactly, and for others by using the SPA. The analytic expression is obtained as [4]

$$g_{m(p,t)}^{(\text{sph})}(k) = 2R_0(kR_0)^{3/2} A_{m(p,t)}^{(\text{sph})} \sin \left(kmL_{pt} - \frac{\pi}{2} \mu_{m(p,t)}^{(\text{sph})} \right), \quad (2.13)$$

with

$$A_{m(p,t)}^{(\text{sph})} = \sin(2\varphi_{pt}) \sqrt{\frac{\sin \varphi_{pt}}{mp\pi}}, \quad \mu_{m(p,t)}^{(\text{sph})} = m(2t - p) - \frac{3}{2}. \quad (2.14)$$

On the other hand, the diameter orbit ($p = 2t$) forms a two-parameter family since the rotation about the diameter itself does not generate a family. The contribution of the diameter family $m(2, 1)$ is also derived from Eq. (2.6) in the same manner as the polygon orbits, and is expressed as [4]

$$g_{m(2,1)}^{(\text{sph})}(k) = 2R_0(kR_0) A_{m(2,1)}^{(\text{sph})} \sin \left(kmL_{21} - \frac{\pi}{2} \mu_{m(2,1)} \right), \quad (2.15)$$

with

$$A_{m(2,1)}^{(\text{sph})} = \frac{1}{2\pi m}, \quad \mu_{m(2,1)} = 2. \quad (2.16)$$

In general, gross shell structure is governed by the contribution of some shortest periodic orbits. In Fig. 1,
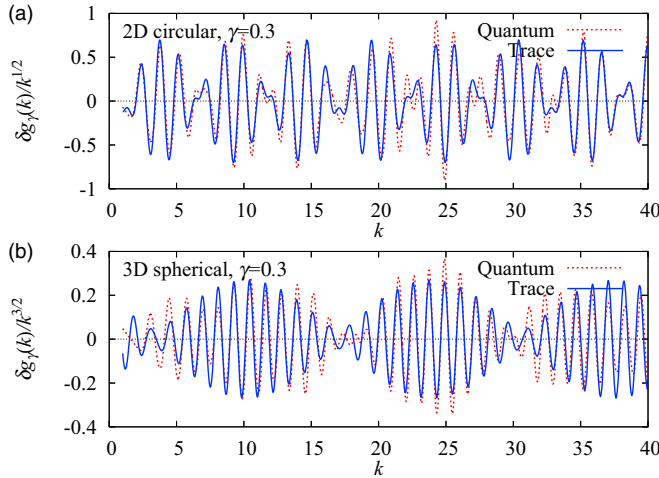
FIG. 1. Oscillating part of the level density with averaging width $\gamma = 0.3$ for (a) 2D circular billiard and (b) 3D spherical cavity systems. In each panel, the dotted (red) line represents the quantum result and the solid (blue) line represents the result of the semiclassical trace formula with the contributions of a few major orbits. For the circular billiard, the contributions of the diameter (2,1) and triangle (3,1) orbit families are taken into account. For the spherical cavity, the contributions of the triangle (3,1) and square (4,1) orbit families are considered.

the oscillating part of the level density averaged with the width γ,

$$\delta g_\gamma(k) = \int dk' [g(k') - \bar{g}(k')] \exp\left[-\frac{1}{2}\left(\frac{k-k'}{\gamma}\right)^2\right],$$
(2.17)

is shown for the 2D circular billiard and the 3D spherical cavity. The smoothing width $\gamma = 0.3$ is taken, for which only the orbits with length $L \lesssim \pi/\gamma \approx 10$ contribute. In the 2D circular billiard, all the periodic orbits form a one-parameter family, and the dominance of their contribution to the gross shell structure is mainly determined by the shortness of the length. In the upper panel of Fig. 1, one sees that the quantum result of $\delta g_\gamma(k)$ for 2D circular billiard is nicely reproduced by the semiclassical formula (2.11) with the contribution of only two shortest orbits, diameter (2,1) and triangle (3,1). In the 3D spherical cavity, the shortest orbit is the diameter, but it plays a minor role compared with the other polygon families due to the low degeneracy. In the lower panel of Fig. 1, the quantum result of $g_\gamma(k)$ for the 3D spherical cavity is compared with the semiclassical trace formula (2.13) taking the contributions of only triangle (3,1) and square (4,1) families into account. One sees that the outstanding beating pattern called supershell structure is successfully reproduced as the interference effect of those two orbits [4]. The agreements of the semiclassical trace formula with the quantum results are already fine with the above two main orbits, and become much better when the contributions of other remaining orbits are incorporated.
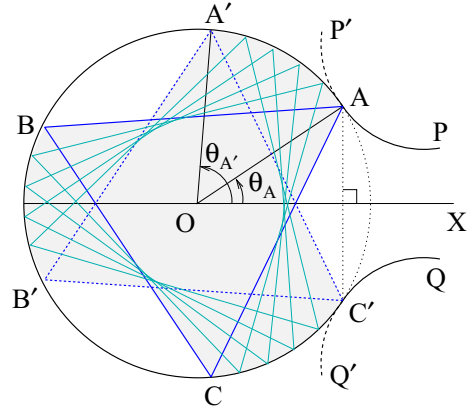

FIG. 2. Degenerate family of triangle orbits in the truncated circular billiard. The circular wall is truncated at the points A and C′, where the wall is smoothly connected to the outer parts AP and C′Q. A continuous family of orbits (p, t) is available for the angles $\theta_A \equiv \angle \text{AOX} < \pi/p$, where OX is the axis of symmetry for the circle wall. For instance, the equilateral triangle orbit (3,1) is possible for $\theta_A < \pi/3$ and forms a continuous family by rotating anticlockwise from ABC to A′B′C′.

B. Two-dimensional truncated circular billiard

Now I consider a 2D billiard system with the wall partly consisting of a circular arc whose central angle is larger than π. In such a billiard potential, one has a degenerate family of diameter orbits confined in the circle part. In general, there exists a family of regular polygon orbits with p vertices when the central angle of the arc is larger than $2\pi(1 - \frac{1}{p})$. As an example, shown in Fig. 2, the rotation around the center O generates a continuous family of triangle orbits (3,1) ranges from ABC to A′B′C′. To avoid the complication due to singularities, I assume that the circle part of the wall is smoothly connected to the neighboring walls AP and C′Q as illustrated in Fig. 2.

Let us consider the contribution of this orbit family to the semiclassical level density based on Eq. (2.6). Fixing the position of the first vertex P_1, the positions of the other vertices of the stationary path are uniquely determined. I take $s_1 = R\theta$ as the position of P_1 and s_j $(j \geqslant 2)$ as the displacement of the jth vertex from its position in the stationary path for given s_1. Figure 3 schematically shows the distribution of periodic orbits on the surface coordinate space $\boldsymbol{s} = (s_1, \ldots, s_p)$. Panel (a) shows a schematic contour plot of the length l_{pt} near the truncated periodic-orbit family. The stationary points of the length l_{pt} give the periodic orbits, and the thick solid line represents the continuous set of stationary points corresponding to the degenerate periodic-orbit family parametrized by the rotation angle θ. It is truncated at $\theta = \theta_A$ and $\theta_{A'}$ indicated by the dots, which correspond to what I call the marginal orbits. I evaluate the integrals in Eq. (2.6) by dividing the integration range into two parts: the interior portion (principal term) and the area around the end points (marginal term). In the interior portion of the family, $\theta_A < \theta < \theta_{A'}$, the orbit length l_{pt} is expanded with respect to $\boldsymbol{s}_\perp = (s_2, \ldots, s_p)$ as

$$l_{pt}(\boldsymbol{s}) = L_{pt} + \frac{1}{4R}\sum_{a,b \geqslant 2} K_{ab} s_a s_b + O(s_\perp^3),$$
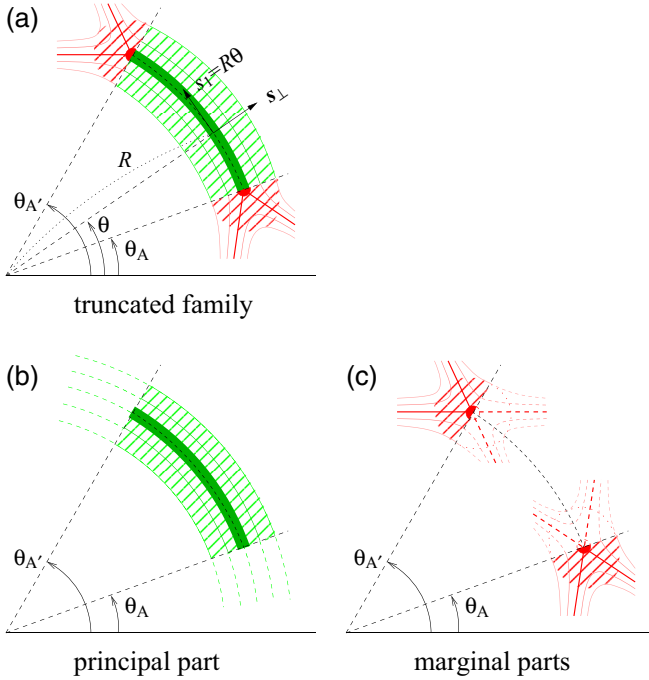(2.18)

FIG. 3. Illustration of the distribution of periodic orbits on the surface coordinate space for truncated circular billiard [panel (a)]. Thin solid lines represent the contour of the orbit length $l_{pt}(s)$, the thick line represents the degenerate periodic-orbit family, and solid dots at the both ends of the family denote the marginal orbits. In the stationary-phase approximation, the shaded area around the family (set of nearly periodic orbits) makes a major contribution to the integral (2.6). In the above area, the part $\theta_A < \theta < \theta_{A'}$ [panel (b)] gives the principal term (2.21), and the terminal semidisc parts around the dots [panel (c)] give the marginal orbit contributions (2.23). The broken lines in panel (c) represent the contour of the orbit length in the case when the wall outside of the circle part is extended toward the inside as AP′, illustrated in Fig. 2.

where K is the $(p-1)$-dimensional curvature matrix defined by

$$K_{ab} = 2R \frac{\partial^2 l_{pt}}{\partial s_a \partial s_b}. \quad (2.19)$$

Integration over $s_1 = R\theta$ is performed exactly and the other integrals over $s_\perp$ are carried out using the SPA. This gives

$$\int ds_1 \cdots ds_p \, e^{ikl_{pt}(s_\perp)}$$

$$= R \, (\theta_{A'} - \theta_A) \frac{(4\pi i R/k)^{(p-1)/2}}{\sqrt{|\det K|}} e^{ikL_{pt} - i\pi n_-/2}, \quad (2.20)$$

where n_- is the number of negative eigenvalues of K. In the above procedure, only the integration range of the parameter θ is different from the case of nontruncated circular billiard. Consequently, one has the contribution of the orbit (p,t) in the truncated circle part as

$$g_{pt}^{(pr)}(k) = f_p g_{pt}^{(circ)}(k), \quad (2.21)$$

where f_p denotes the relative volume of the parameter space occupied by the truncated family of orbit compared with that

for the nontruncated circular billiard,

$$f_p = \frac{\theta_{A'} - \theta_A}{2\pi/p} = 1 - \frac{p}{\pi} \theta_A. \quad (2.22)$$

The term given by (2.21), which will be referred to as the principal term, corresponds to the contribution of the shaded area shown in Fig. 3(b).

Since the above family is truncated at $\theta = \theta_A$ and θ'_A, integration over θ in the outer region ($\theta < \theta_A$ and $\theta > \theta_{A'}$) should also be executed using the SPA, and it gives the end-point corrections to the principal contribution. In calculating the end-point corrections, the first vertex of the orbit is supposed to be on the edge of the circle wall, and its stability is calculated for the outer wall neighboring the circle part. In practice, the outer wall is extended into the interior region ($\theta > \theta_A$ and $\theta < \theta_{A'}$) for this vertex, as illustrated with thick broken lines AP′ and C′Q in Fig. 2, so that the curvature of the surface is continuous there. Then the contour plot of the orbit length looks like that shown in Fig. 3(c), and the orbits at the end of the family become isolated. For these hypothetical isolated orbits, which I call marginal orbits, it is possible to calculate their monodromy matrices and Maslov indices in a standard numerical prescription. Thus, the end-point correction to the truncated family contribution, from the shaded area shown in Fig. 3(c), is given by the half of the Gutzwiller formula (2.10) for each of those isolated marginal orbits β as

$$g_{pt,\beta}^{(mg)}(k) = 2R A_{pt,\beta}^{(mg)} \sin\left(kL_{pt} - \frac{\pi}{2}\mu'_{pt,\beta}\right), \quad (2.23)$$

with the amplitude

$$2R A_{pt,\beta}^{(mg)} = \frac{w_{pt} L_{pt}}{2\pi \sqrt{|\det(M_{pt,\beta} - I)|}}. \quad (2.24)$$

In Eq. (2.23), the sine function is taken for the definition of the Maslov index, in contrast to the cosine one in Eq. (2.10), in accord with Eq. (2.11).

Finally, the total contribution of the family of orbit (p,t) confined in the circle part is given by the sum of the principal and marginal terms as

$$g_{pt}^{(tot)}(k) = g_{pt}^{(pr)}(k) + \sum_\beta g_{pt,\beta}^{(mg)}(k), \quad (2.25)$$

where the sum in the second term is taken over the two marginal orbits β.

C. Three-dimensional truncated spherical cavity

Next I consider a 3D cavity potential whose wall partly consists of a truncated sphere with radius R. As shown in Fig. 4, the spherical part is centered at O, truncated with the plane perpendicular to the axis OZ, and smoothly connected to the neighboring part of the surface, which is assumed to be axially symmetric about the axis OZ. In the truncated spherical cavity, one has the same set of periodic-orbit families as in the complete (nontruncated) spherical cavity, but with the restricted ranges of the parameters.

For instance, consider a family of triangle orbits confined in the spherical part as shown in Fig. 4. The position of the first vertex P$_1$ is determined by the polar angle ϑ_1 and azimuthal
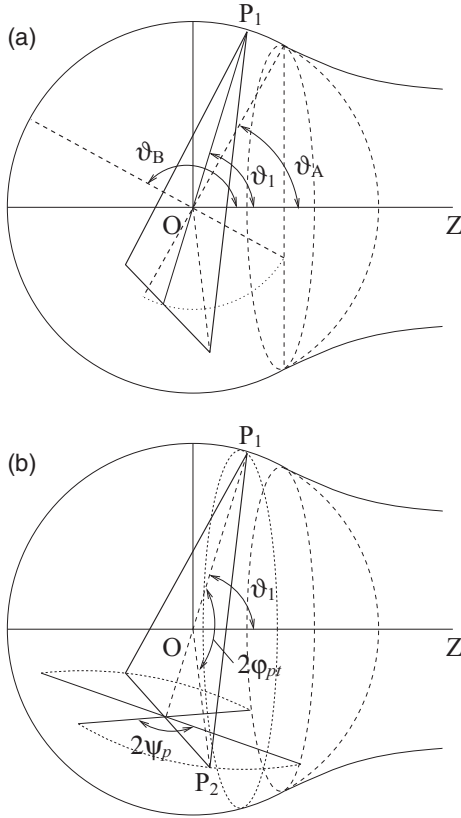
(a)

(b)

FIG. 4. Geometry of the periodic-orbit family confined in the 3D truncated spherical cavity potential. The top panel (a) shows the range of the angle ϑ_1 of the first vertex P$_1$, which can vary from ϑ_A to ϑ_B. For a given value of ϑ_1, the orbit can rotate 2π around the symmetry axis OZ. The orbit can be also rotated about the axis OP$_1$, and the bottom panel (b) shows the range ψ_p for this rotation which is dependent on ϑ_1.

angle φ_1 around the symmetry axis OZ. One obviously has a restriction on the polar angle, $\vartheta_A < \vartheta_1 < \vartheta_B$, as shown in Fig. 4(a), so that the entire orbit fits the confines in the spherical part. In general, the maximum angle ϑ_B for the orbit (p, t) is given by

$$
\vartheta_B = \begin{cases} \pi - \vartheta_A & \text{for even } p, \\ \pi & \text{for odd } p \text{ with } \vartheta_A \leqslant \frac{\pi}{p}, \\ \cos^{-1}\left[-\frac{\cos\vartheta_A}{\cos(\pi/p)}\right] & \text{for odd } p \text{ with } \vartheta_A > \frac{\pi}{p}. \end{cases}
$$
(2.26)

Let us consider the principal part of the integrals in Eq. (2.6), taking into account the degeneracies of the orbit. As illustrated in Fig. 5, the local surface coordinates (x_a, y_a) are defined on the surface S around the vertex P$_a$ of a given periodic orbit, where x_a is taken along the orbital plane N_a, and y_a perpendicular to it.

Let us first consider a diameter family $(2,1)$. In this case, the orbit in the family is uniquely specified by fixing the position of the first vertex P$_1$, and the coordinates (x_1, y_1) are varied in the available range, which fixes the orbit in the family. Then, in Eq. (2.6), the integrals over (x_1, y_1) are done
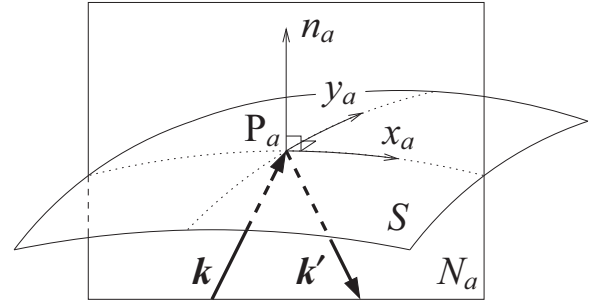

FIG. 5. Definition of the local coordinates around the vertex P$_a$ on the surface S. $\boldsymbol{k}$ and $\boldsymbol{k'}$ represent the wave vectors before and after reflection at P$_a$, and they define the orbital plane N_a. (x_a, y_a) are local surface coordinates tangent to S, where x_a is taken in the orbital plane N_a and y_a orthogonal to x_a. n_a is normal to S toward exterior region.

exactly so as to include all members of the family, and the other $(2p - 2)$ integrals are carried out using the SPA. The integration over $(x_1 = R\vartheta_1, \ y_1 = R\varphi_1 \sin\vartheta_1)$ gives

$$
\int dx_1 dy_1 = \int R \, d\vartheta_1 \, R \sin\vartheta_1 d\varphi_1
$$
$$
= 2\pi R^2 \int_{\vartheta_A}^{\pi - \vartheta_A} \sin\vartheta \, d\vartheta = 4\pi R^2 \cos\vartheta_A.
$$
(2.27)

I define f_2 as the relative volume of the parameter space occupied by the truncated diameter family compared with that for the complete (nontruncated) spherical cavity, which will be called "occupation rate" for brevity. Since the same integral as (2.27) in the complete spherical cavity gives the factor $4\pi R^2$, one obtains

$$
f_2 = \cos\vartheta_A.
$$
(2.28)

Since the remaining $(2p - 2)$ integrals using the SPA give a result equivalent to that for the complete spherical cavity, the principal contribution of the truncated diameter family is given by

$$
g_{m(2,1)}^{\text{(pr)}}(k) = f_2 g_{m(2,1)}^{\text{(sph)}}(k),
$$
(2.29)

with $g_{m(2,1)}^{\text{(sph)}}(k)$ given by Eq. (2.15).

For polygon family (p, t) $(p > 2t)$, after fixing the first vertex P$_1$, one can further rotate the orbit about the axis OP$_1$ as shown in Fig. 4(b). I define the rotation angle ψ of the orbital plane around the axis OP$_1$ measured from the position where it is perpendicular to the plane defined by the symmetry axis OZ and the rotation axis OP$_1$. Its maximum value ψ_p is given by

$$
\sin\psi_p(\vartheta_1) = \frac{\cos\vartheta_A - \cos(2\pi j/p)\cos\vartheta_1}{\sin(2\pi j/p)\sin\vartheta_1},
$$
(2.30)

if the vertex P$_{j+1}$ with $\angle$P$_1$OP$_{j+1} = 2\pi j/p$ first touches the joint circle by the above rotation. If no vertices touch the joint with the rotation, one simply has $\psi_p = \pi/2$. Thus, for the polygon family, the integrals in (2.6) should be done exactly for three coordinates: $x_1 = R\vartheta_1$, $y_1 = R\varphi_1 \sin\vartheta_1$, and

$y_2 = R\psi \sin(2\varphi_{pt})$. For a given (x_1, y_1), the integral over ψ simply gives $4\psi_p(\vartheta_1)$, and one obtains

$$\int dx_1 dy_1 dy_2 = \int R d\vartheta_1\, R\sin\vartheta_1 d\varphi_1\, R\sin(2\varphi_{pt})d\psi$$
$$= 8\pi R^3 \sin(2\varphi_{pt}) \int_{\vartheta_A}^{\vartheta_B} \psi_p(\vartheta)\sin\vartheta\, d\vartheta. \quad (2.31)$$

Since the same integral for the complete spherical cavity gives $8\pi R^3 \sin(2\varphi_{pt})$, one obtains the occupation rate f_p for the family (p, t) as

$$f_p = \int_{\vartheta_A}^{\vartheta_B} \psi_p(\vartheta)\sin\vartheta\, d\vartheta. \quad (2.32)$$

The remaining $(2p - 3)$ integrations in (2.6) using the SPA give exactly the same results as those for the complete spherical cavity, and the principal contribution of the polygon family (p, t) to the level density is expressed as

$$g_{pt}^{(pr)}(k) = f_p g_{pt}^{(sph)}(k) \quad (2.33)$$

with $g_{pt}^{(sph)}(k)$ given by Eq. (2.13).

In addition to the above principal terms, one should consider the end-point corrections. They are associated with the marginal orbits whose first vertex P_1 is on the joint of the spherical and the neighboring walls as shown in Fig. 6. For such orbits, the local surface coordinate (x_1, y_1) is transformed into (ξ_1, η_1) so that ξ_1 is along the joint circle and η_1 perpendicular to it along the surface outside the spherical wall, as illustrated in Fig. 6. Then, the integral over $\eta_1 > 0$ is executed using the SPA. The contribution of the marginal orbit is obtained, just in the same manner as the billiard case, by extending the wall neighboring the spherical part into the inner region around P_1 so that the curvature of the surface is continuous there. It makes the marginal orbits a family with reduced degeneracy whose symmetry-reduced monodromy matrices and Maslov indices can be calculated in the standard prescription. For the marginal diameter family, which forms a one-parameter family generated by the rotation about the symmetry axis, the integral over ξ_1 is executed exactly and the rest of the $(2p - 1)$ integrals are carried out using the SPA.
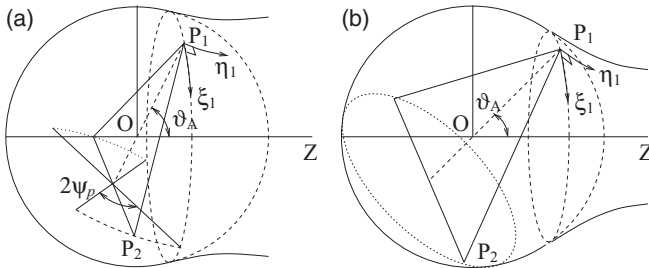

FIG. 6. Local coordinates for a marginal orbit with its vertex P_1 on the joint. Around the vertex P_1, local coordinate ξ_1 is taken along the joint circle and η_1 perpendicular to it. For ϑ_A close to $\pi/2$, the vertex P_2 touches the joint circle by rotating the orbit about the axis OP_1 [panel (a)], but it can rotate 2π around the axis OP_1 for sufficiently small ϑ_A [panel (b)].

The contribution to the level density is expressed in the form

$$g_{21}^{(mg)}(k) = 2R\sqrt{kR} A_{21}^{(mg)} \sin\left(kL_{21} - \frac{\pi}{2}\mu'_{21}\right), \quad (2.34)$$

where $A_{21}^{(mg)}$ represents the dimensionless energy-independent amplitude factor. For the marginal polygon family, which forms a two-parameter family, the integrals with respect to (ξ_1, y_j) are executed exactly and the rest of the $2p$ integrals are carried out by using the SPA. The result is expressed in the form

$$g_{pt}^{(mg)}(k) = 2R(kR)A_{pt}^{(mg)} \sin\left(kL_{pt} - \frac{\pi}{2}\mu'_{pt}\right). \quad (2.35)$$

See the Appendix for the expressions of the amplitude factors $A_{pt}^{(mg)}$.

For a marginal polygon family for which Eq. (2.30) gives the angle $\psi_p(\vartheta_A) < \pi/2$, one should consider a secondary marginal orbit which has two vertices P_1 and P_j on the joint. It forms a one-parameter family, and its contribution is evaluated by executing the integral over ξ_1 exactly and the other $(2p - 1)$ integrals through the SPA to obtain

$$g_{pt}^{(mm)}(k) = 2R\sqrt{kR} A_{pt}^{(mm)} \sin\left(kL_{pt} - \frac{\pi}{2}\mu''_{pt}\right). \quad (2.36)$$

The expression of the amplitude factor $A_{pt}^{(mm)}$ is also given in the Appendix.

Finally, the total contribution of the family of orbit (p, t) confined in the spherical part of the wall is given by

$$g_{pt}^{(tot)}(k) = g_{pt}^{(pr)}(k) + g_{pt}^{(mg)}(k) + g_{pt}^{(mm)}(k). \quad (2.37)$$

III. APPLICATIONS TO THE THREE-QUADRATIC-SURFACES POTENTIALS

A. The three-quadratic-surfaces parametrization

As the applications of the trace formula obtained above, I consider the 2D billiard as well as the axially symmetric 3D cavity with the three-quadratic-surfaces (TQS) parametrization [24], which is designed to describe nuclear fission processes. The cavity potential is known to preserve the important characteristics of single-particle shell structures in more realistic nuclear mean-field models such as the Woods-Saxon potential with spin-orbit coupling [7]. Thus, the results obtained with this model will help one understand some essential features of the fission dynamics at least qualitatively.

The potential wall consists of the two prefragment parts and the neck part between them as shown in Fig. 7, and each of those three parts is given by the axially symmetric quadratic surface $\rho = \rho_s(z)$ expressed as

$$\rho_s^2(z) = \begin{cases} a_1^2 - \dfrac{a_1^2}{c_1^2}(z - l_1)^2 & (z_{\min} < z < z_1), \\[2mm] a_3^2 - \dfrac{a_3^2}{c_3^2}(z - l_3)^2 & (z_1 < z < z_2), \\[2mm] a_2^2 - \dfrac{a_2^2}{c_2^2}(z - l_2)^2 & (z_2 < z < z_{\max}). \end{cases} \quad (3.1)$$

On the right-hand side, the first and third lines describe the left and right prefragments centered at $z = l_1$ and l_2. The second line describes the neck part, which is smoothly connected to
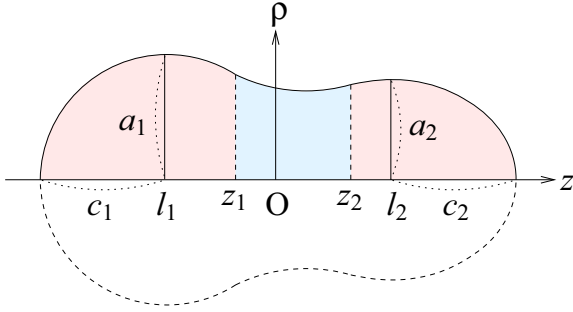
FIG. 7. TQS parametrization for the shape of the nuclear fission process; see Eq. (3.1) for the parameters.

the left and right prefragments at $z = z_1$ and z_2, respectively. Note that the neck part is concave in most cases, for which one has $c_3^2 < 0$. The continuity of $\rho_s(z)$ and $\rho_s'(z)$ at the joints $z = z_1$ and z_2 impose four constraints on the eleven parameters $\{a_{1-3}, c_{1-3}, l_{1-3}, z_{1,2}\}$, and the center-of-mass and volume conservation conditions impose two more constraints. (The last two conditions are imposed assuming the 3D axial cavity, and I use the same values of the parameters also in the 2D billiard.) Thus, one eventually has five free parameters which describe the shape of the potential. Among the useful choices for the shape parameters [24] are $\{\sigma_{1-3}, \alpha_{1-3}\}$ defined by

$$
\begin{aligned}
\sigma_1 &= \frac{l_2 - l_1}{u}, \quad \alpha_1 = \frac{l_1 + l_2}{2u} \quad \text{with} \quad u = \sqrt{\frac{a_1^2 + a_2^2}{2}}, \\
\sigma_2 &= d\frac{a_3^2}{c_3^2}, \quad \alpha_2 = \frac{a_1^2 - a_2^2}{u^2}, \\
\sigma_3 &= \frac{1}{2}\left(\frac{a_1^2}{c_1^2} + \frac{a_2^2}{c_2^2}\right), \quad \alpha_3 = \frac{a_1^2}{c_1^2} - \frac{a_2^2}{c_2^2}.
\end{aligned} \tag{3.2}
$$

The parameter σ_1 describes the elongation, σ_2 gives the neck curvature, α_2 is related to the fragment-mass asymmetry, and σ_3 and α_3 determine the shapes of the prefragments. The parameter α_1 represents the asymmetry of the positions of the prefragments from the center of mass, and it is automatically determined by the other 5 parameters. In this paper, I only consider the case of symmetric shapes ($\alpha_{1-3} = 0$) with fixed neck curvature ($\sigma_2 = -0.6$) and spherical prefragments ($\sigma_3 = 1$). The shapes of the wall for several values of σ_1 are shown in Fig. 8. Results for asymmetric shapes, which are significant in investigating the origin of asymmetric fission, will be presented in a separate paper [25].
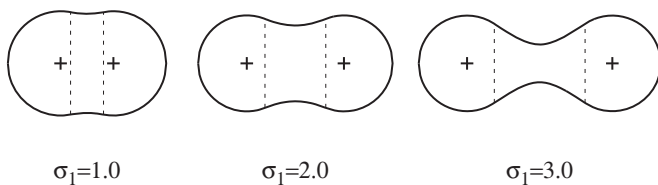

FIG. 8. Shapes of the symmetric TQS wall with $\sigma_2 = -0.6$, $\sigma_3 = 1$, and several values of the elongation parameter σ_1.

B. Classical periodic orbits in the TQS wall

I discuss here the properties of classical periodic orbits in the TQS billiard and cavity potentials. Let us first consider the 2D billiard system. Since the TQS wall under consideration consists partly of circular arcs, one has a degenerate family of orbits confined in each of them. The radius of the circle is $a_1 = c_1 \equiv R$ and the angle θ_A in Fig. 2 for the TQS model is given by

$$
\cos\theta_A = \frac{z_1 - l_1}{R}. \tag{3.3}
$$

The diameter orbit is the only degenerate family confined in the prefragment part in the deformation range $0 \leqslant \sigma_1 \leqslant 2.5$, for which θ_A is always greater than $\pi/3$. The triangle family appears at $\sigma_1 \simeq 2.67$ and the square family at $\sigma_1 \simeq 3.78$.

Besides the degenerate family in the prefragments, there are isolated orbits which hit the neck part of the wall or go back and forth between two prefragments. Some of those isolated orbits for $\sigma_1 = 2.0$ are shown in Fig. 9. Since the neck part has negative curvature, the orbits reflected on the neck surface are strongly unstable (chaotic) and are expected to make only a small contribution to the level density. Figure 10 shows the stability factor $1/\sqrt{|\det(\mathsf{M}_\beta - I)|}$ in the Gutzwiller trace formula (2.10) for some short isolated orbits shown in Fig. 9. For the orbits 3Rb and 4Rb, which have vertices on the neck part, the value of the stability factor is considerably smaller than those for the orbits 3Ra and 4Ra, which have vertices only on the prefragment parts. One sees that the latter also become chaotic with increasing elongation parameter σ_1.

In the 3D TQS cavity potential, one has families of all the regular polygons (p, t) confined in the spherical prefragment parts. As in the nontruncated spherical cavity, the polygon orbits $(p > 2t)$ form three-parameter families and the diameter orbits $(p = 2t)$ form two-parameter families. The orbits shown in Fig. 9 in this case will form a one-parameter family generated by the rotation about the symmetry axis, except the
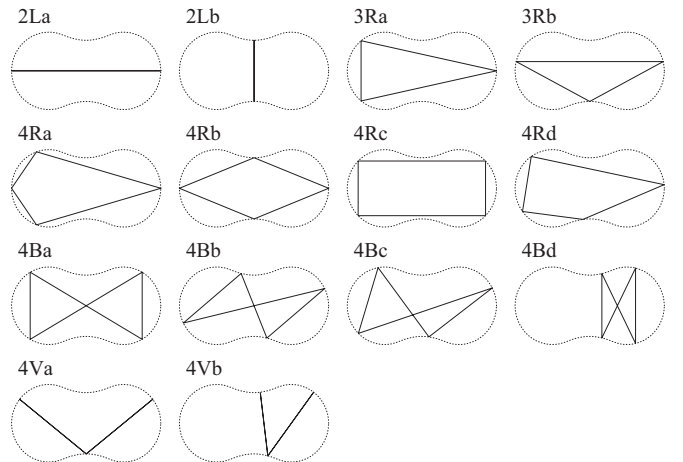

FIG. 9. Some short isolated periodic orbits in the symmetric TQS billiard potential for $\sigma_1 = 2.0$, $\sigma_2 = -0.6$, and $\sigma_3 = 1$. The name of the orbit is given after the number of vertices, the type of the shape (abbreviation of linear, rotational, butterfly, or V shaped), and an alphabetic identifier.
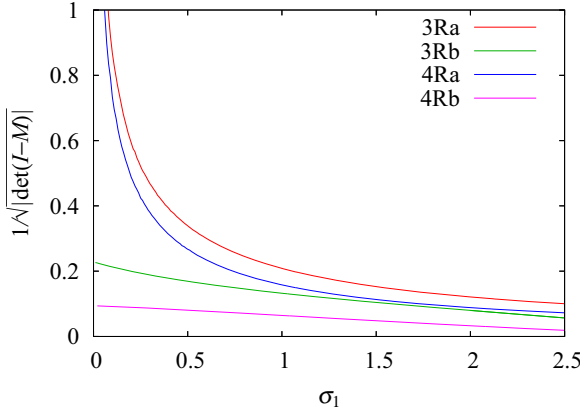
FIG. 10. Stability factor $1/\sqrt{|\det(M_\beta - I)|}$ for several isolated periodic orbits shown in Fig. 9.

diameter 2La which remains isolated. In addition, one has orbits on the equatorial plane in the neck surface and three-dimensional orbits, which also form one-parameter families. From the viewpoint of semiclassical expansion with respect to the degeneracy, the shell effect might be mainly governed by the three-parameter polygon families in the prefragments, with relatively small contribution of the two-parameter diameter family, and the other one-parameter families might play only minor roles.

C. Fourier analysis

In the billiard and cavity systems, the action integral along the orbit is given by a simple product of the wave number k and the orbit length L_β. Owing to such a simple energy dependence of the phase part, one obtains a clear correspondence between the classical periodic orbits and quantum level density through the Fourier analyses. The Fourier transform of the level density defined by

$$F(L) = \sqrt{\frac{2}{\pi}} \int_0^\infty dk \, g(k) e^{ikL} e^{-(k/k_c)^2/2} \qquad (3.4)$$

is considered, where a Gaussian factor with the cutoff momentum k_c is introduced in the integrand to truncate the high energy part $k \gg k_c$ of the level density unavailable in the numerical calculation. Inserting the quantum level density $g(k) = \sum_i \delta(k - k_i)$, one has

$$F^{(\mathrm{qm})}(L) = \sqrt{\frac{2}{\pi}} \sum_i e^{ik_i L} e^{-(k_i/k_c)^2/2} \qquad (3.5)$$

which can be easily evaluated using the quantum spectrum. The semiclassical level density in a hard-wall potential model (either in 2D or 3D) is generally expressed in a form

$$g(k) = g_0(k) + 2R_0 \sum_\beta (kR_0)^{D_\beta/2} A_\beta \sin\left(kL_\beta - \frac{\pi}{2}\mu_\beta\right), \qquad (3.6)$$
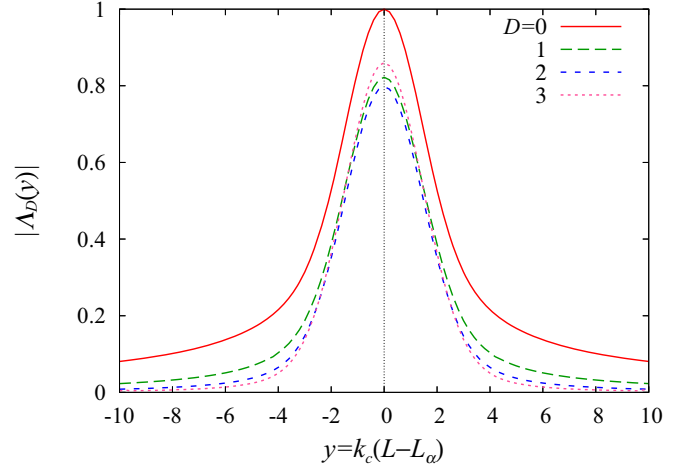

FIG. 11. Modulus of the function $\Lambda_D(y)$ defined by Eq. (3.8) for several values of D.

where D_β is the degeneracy of the orbit family β. Inserting (3.6) into (3.4), one has

$$F^{(\mathrm{sc})}(L) = F_0(L) + i \sum_\beta (k_c R_0)^{1+D_\beta/2} A_\beta e^{i\pi\mu_\beta/2}$$

$$\times \Lambda_{D_\beta}(k_c(L - L_\beta)), \qquad (3.7)$$

where

$$\Lambda_D(y) = \sqrt{\frac{2}{\pi}} \int_0^\infty dx \, x^{D/2} e^{iyx} e^{-x^2/2} \qquad (3.8)$$

is a function whose modulus has a peak at the origin $y = 0$ as shown in Fig. 11. Thus, the Fourier amplitude of the quantum level density calculated with Eq. (3.5) will exhibit successive peaks at the lengths of classical periodic orbits, whose heights are proportional to the amplitude factor A_β of the semiclassical level density. If the cutoff momentum k_c is large enough to single out the peak of the orbit β from those of the other orbits, the modulus of the Fourier transform at $L = L_\beta$ is given by

$$|F(L_\beta)| = (k_c R_0)^{1+D_\beta/2} \Lambda_{D_\beta}(0) A_\beta, \qquad (3.9)$$

$$\Lambda_D(0) = \frac{2^{D/2} \Gamma(1 + D/2)}{\sqrt{\pi}}. \qquad (3.10)$$

Taking account of all the marginal families, the contribution of the orbit (p, t) to the level density of the truncated circular billiard or the truncated spherical cavity is written as

$$g_{pt}(k) = 2R \sum_D (kR)^{D/2} A_{pt}^{(D)} \sin\left(kL_{pt} - \frac{\pi}{2}\mu_{pt}^{(D)}\right), \quad (3.11)$$

where the sum is taken over the degeneracy parameters D which differ in principal and marginal terms (see the Appendix). It can be written in a more compact way as

$$g_{pt}(k) = 2R |\mathcal{A}_{pt}(kR)| \sin\left(kL_{pt} - \frac{\pi}{2}\mu_{pt}^{(\mathrm{eff})}\right), \qquad (3.12)$$

with the complex amplitude $\mathcal{A}_{pt}$ and effective Maslov index $\mu_{pt}^{(\text{eff})}$ defined by

$$\mathcal{A}_{pt}(x) = \sum_D x^{D/2} A_{pt}^{(D)} e^{-i\pi\mu_{pt}^{(D)}/2}, \qquad (3.13)$$

$$-\frac{\pi}{2}\mu_{pt}^{(\text{eff})}(x) = \arg \mathcal{A}_{pt}(x). \qquad (3.14)$$

The Fourier transform at $L = L_{pt}$ is then given by

$$F(L_{pt}) = i \sum_D (k_c R)^{1+D/2} e^{i\pi\mu_{pt}^{(D)}/2} \Lambda_D(0) A_{pt}^{(D)} \qquad (3.15)$$

$$\approx 0.8 i k_c R \mathcal{A}_{pt}^*(k_c R). \qquad (3.16)$$

In the last approximation, the value $\Lambda_{D\geqslant 1}(0) \approx 0.8$ is used, which can be seen in Fig. 11. Thus, the Fourier transform of the quantum level density provides us with direct information on the amplitude $\mathcal{A}_{pt}$, which represents the combined contribution of the principal and marginal terms.

D. Two-dimensional TQS billiard

In this section, the quantum-classical correspondence in the 2D TQS billiard system is investigated using the Fourier transformation technique discussed above. In the top panel of Fig. 12, moduli of the quantum Fourier transform $|F^{(\text{qm})}(L; \sigma_1)|$ are displayed as functions of L and σ_1. In the bottom panel, lengths of some classical periodic orbits are plotted as functions of σ_1. As expected from the semiclassical trace formula, Fourier amplitudes of the quantum level density show peaks at the lengths of the classical periodic orbits. For the circular shape ($\sigma_1 = 0$), one sees strong Fourier peaks at $L = L_{21}(= 4)$, $L_{31}(= 3\sqrt{3} \simeq 5.19)$, and $L_{41}(= 4\sqrt{2} \simeq 5.66)$ corresponding to the diameter, triangle, and square orbits, respectively. Those peaks promptly decay with increasing σ_1, but the peak of the prefragment diameter orbits (labeled 2F) grows again at large σ_1.

Figure 13 shows the Fourier amplitude $|F(L_{21}(\sigma_1))|$ evaluated at the length of the diameter orbit as functions of the deformation parameter σ_1. The quantum mechanical result is compared with the semiclassical one given by (3.16). It is found that the principal term considerably underestimates the quantum result in the energy region considered, especially for the case of small σ_1. After taking into account the contributions of the marginal orbits, the quantum result is reasonably reproduced for $\sigma_1 \gtrsim 1.0$. For smaller σ_1, the breaking of the total rotational symmetry should be treated appropriately using a kind of uniform approximation, but it is beyond the scope of the current work.

Figure 14 shows the oscillating part of the quantum and semiclassical level densities (2.17) for TQS billiard with the deformation parameter $\sigma_1 = 1.0$ and 2.0. Values of the averaging width $\gamma = 0.2$ and 0.5 are used to see the fine and gross shell structures, respectively. In each panel, one sees that the quantum results are nicely reproduced by the semiclassical trace formulas, taking account of the contribution of short isolated orbits shown in Fig. 9 as well as the prefragment diameter families. The contributions of the isolated orbits are calculated with the Gutzwiller formula (2.10). In the contribution of the prefragment diameter families, both principal and
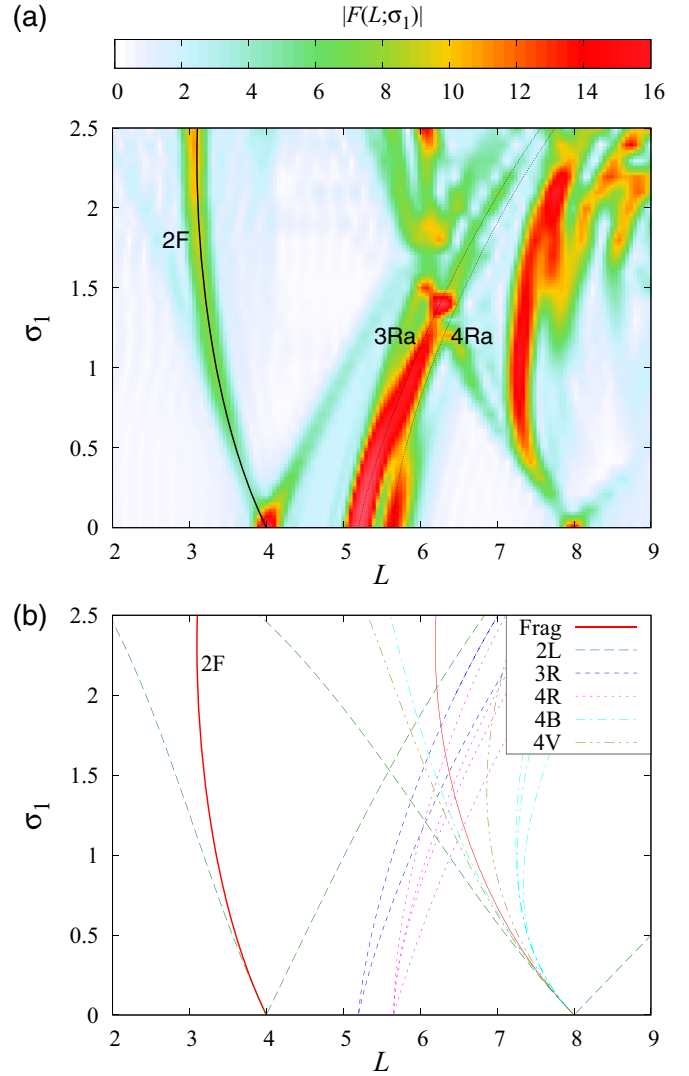
FIG. 12. The top panel (a) shows the Fourier amplitude of the quantum level density as a function of L (abscissa) and σ_1 (ordinate). In the bottom panel, lengths of the classical periodic orbits are plotted as functions of σ_1 in the same range of (σ_1, L) as the top panel. The solid line labeled 2F represents the diameter orbit family confined in the prefragments. Broken lines represent the isolated orbits as shown in Fig. 9.

marginal terms are taken into account. As shown in the plots for $\gamma = 0.5$, the contribution of the primitive diameter orbit family dominates the gross shell structures.

E. Three-dimensional TQS cavity

Next, let us consider the 3D TQS cavity systems. Unlike the 2D billiard, one has all (p, t) families confined in the spherical prefragments for all values of $\sigma_1 > 0$. The principal contributions of the three-parameter polygon families ($p > 2t$) and two-parameter diameter families ($p = 2t$) are obtained with the occupation rate f_p given by Eqs. (2.32) and
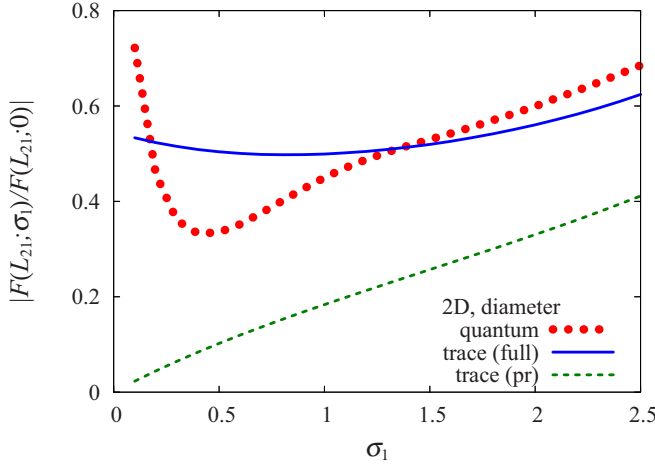
FIG. 13. Fourier amplitudes of the level density for the TQS billiard evaluated at the length of the diameter orbit confined in the circle parts. Its value relative to that for the spherical shape is plotted as a function of σ_1. The thick dotted (red) line represents the quantum result, and the solid (blue) line represents the result of the semiclassical trace formula, taking account of the marginal orbit contributions. The dashed (green) line shows the semiclassical result only with the contribution of the principal family.

(2.28) as

$$g_{pt}^{(pr)}(k;\sigma_1) = 2 \sum_{pt} f_p g_{pt}^{(sph)}(k; R(\sigma_1)), \qquad (3.17)$$

where $g_{pt}^{(sph)}(k; R)$ represents the contribution of the orbit family (p, t) in the spherical cavity with radius R, and the overall factor 2 counts the families in two prefragments which are equivalent for the symmetric shapes. Numerical results of the occupation rate f_p for the symmetric TQS cavity with $\sigma_2 = -0.6$, $\sigma_3 = 1$, $\alpha_{1-3} = 0$ and several values of σ_1 are shown in Table I. With increasing σ_1, the angle ϑ_A indicated in Fig. 4 becomes smaller. Then the occupation rates f_p increase, making the contribution of the prefragment orbit family more important.

To quantify the contributions of the periodic orbits, let us examine the Fourier transform of the level density (3.4) just as in the 2D billiard case. In Fig. 15, the upper panel shows the Fourier amplitude $|F(L;\sigma_1)|$ of the quantum level density as a function of L and σ_1, and the lower panel shows the lengths of the classical periodic orbits L_β as functions of σ_1 in the same ranges of (L, σ_1) as the upper panel. At the spherical shape ($\sigma_1 = 0$), one finds especially large peaks corresponding to the triangle and square orbits, and the peak of the diameter orbit is relatively small due to the lower degeneracy [note the factor $(k_c R_0)^{D_\beta/2}$ in Eq. (3.7)]. With increasing σ_1, those peaks promptly decay, and then the peaks corresponding to the prefragment orbit families begin to grow up. Especially, one sees a remarkable peak at the triangle family (labeled 3F).

Quantum and semiclassical results for the Fourier amplitude $|F(L_{pt})|$ at the lengths of classical periodic orbits (p, t), relative to those for the spherical cavity are shown in Fig. 16. Similarly to the 2D billiard case, the principal term considerably underestimates the quantum Fourier amplitude.
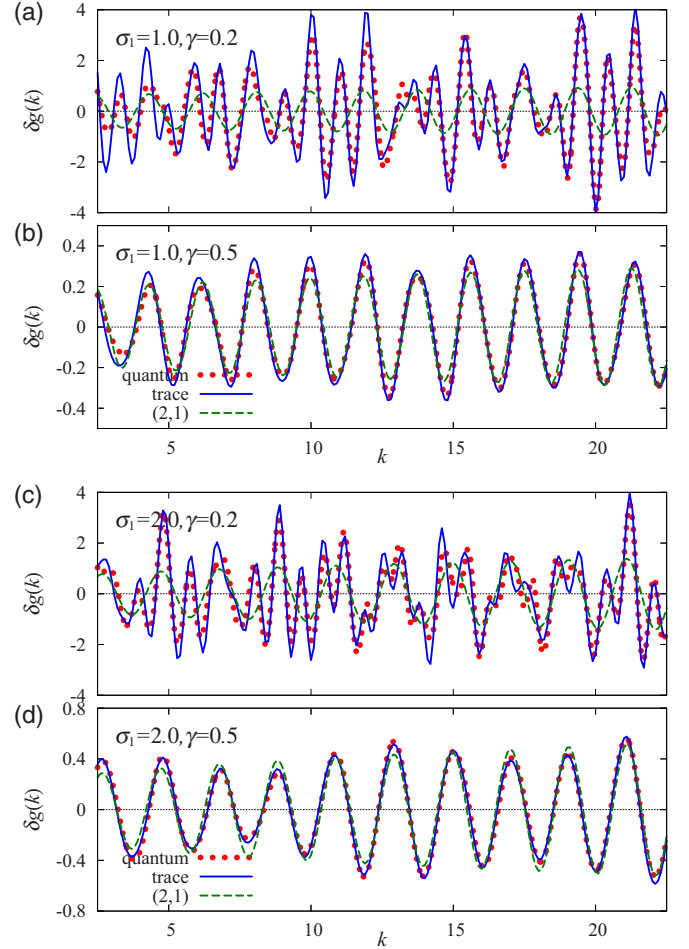

FIG. 14. Oscillating part of the level density with averaging widths $\gamma = 0.2$ and 0.5 for $\sigma_1 = 1.0$ [panels (a) and (b)] and 2.0 [panels (c) and (d)]. Thick dotted (red) lines represent the quantum results, solid (blue) lines represent the trace formula, and broken (green) lines show the contribution of the prefragment diameter orbit family (2,1).

By taking into account the marginal terms, quantum results are nicely reproduced for both diameter and triangle orbits. In the figure for diameter orbits, ragged behavior of the quantum Fourier amplitude might be due to the interference with the other periodic orbits, since the lengths of some equatorial or-

TABLE I. Occupation rate (2.28) and (2.32) for the prefragment orbit families in the symmetric TQS cavity with the parameters $\sigma_2 = -0.6$, $\sigma_3 = 1$ and several values of σ_1. ϑ_A is the angle indicated in Fig. 4.

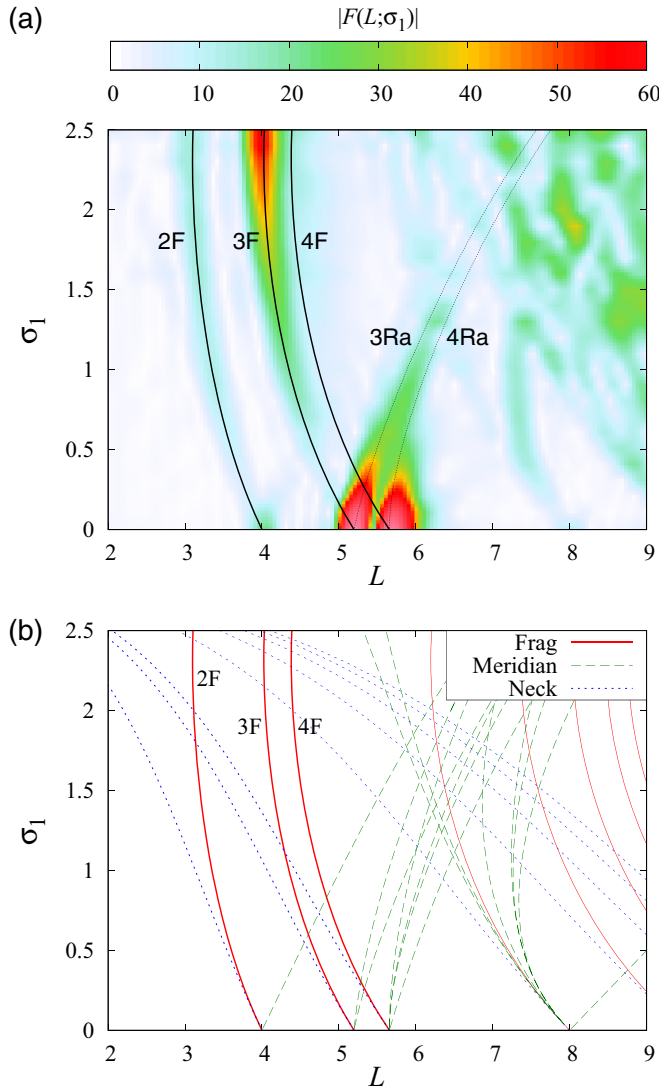| σ_1	1.0	1.5	2.0	2.5	3.0
ϑ_A (deg)	79.193	73.665	67.975	62.047	55.771
f_2	0.18760	0.28088	0.37562	0.46851	0.56190
f_3	0.02962	0.06823	0.12650	0.21112	0.34345
f_4	0.02266	0.05169	0.09436	0.15204	0.22924
f_5	0.02055	0.04683	0.08504	0.13652	0.20416

FIG. 15. Same as Fig. 12 but for the three-dimensional TQS cavity potential model. Solid lines labeled 2F, 3F, and 4F represent the lengths of prefragment diameter, triangle, and square orbits, respectively. Broken lines represent the meridian-plane orbits as shown in Fig. 9. Dotted lines represent the equatorial orbits in the neck part.
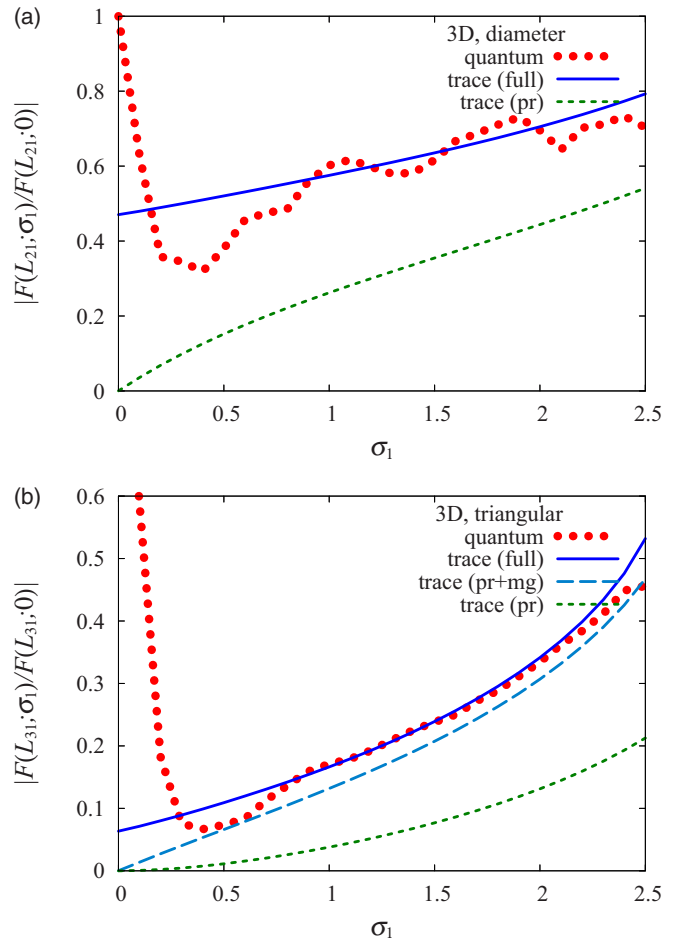

FIG. 16. Same as Fig. 13 but for the diameter (a) and triangle (b) orbits in the three-dimensional TQS cavity potential. In both panels, the thick dotted (red) line represents the quantum result, the solid (blue) line represents the result of the semiclassical trace formula, taking account of all the marginal orbit contributions, and the short-dashed (green) line represents the contribution of the principal family. In the panel (b), the long-dashed (light blue) line represents the result considering the principal family and the marginal orbits, but without the secondary marginal orbits.

bits on the neck surface cross with that of the the prefragment diameter around $\sigma_1 \sim 2$ as seen in Fig. 15(b).

As shown in Fig. 16(b), contribution of the secondary-marginal orbit is considerably smaller than the principal and marginal contributions. The contributions of other one-parameter families such as those shown in Fig. 9 are expected to be of the same order as the secondary-marginal family, and it may not be so bad just to ignore them for simplicity. It is also justified from the Fourier spectrum shown in Fig. 15(a) where one finds no significant peaks along those orbits. Thus, one can consider the semiclassical level density simply with the prefragment periodic-orbit families.

In Fig. 17, quantum level density is compared with the semiclassical trace formula including the contributions of

prefragment diameter (2,1) and polygon families $(p, 1)$ with $3 \leqslant p \leqslant 5$. In these calculations, the averaging width is taken as $\gamma = 0.3$. For every value of deformation σ_1, quantum results are nicely reproduced by the contributions of those prefragment-orbit families. One also sees that the quantum fluctuations are mostly attributed to the contribution of the triangle family for large σ_1 where the neck is well developed. This can be understood from the fact that the triangle orbits are the shortest among the families with the largest degeneracy, and they also have the largest value of the occupation rate f_p among them, as shown in Table I.

IV. SUMMARY AND CONCLUSION

Based on the Balian-Bloch formula, I have derived the contribution of degenerate families of orbits confined in 2D truncated circular billiard and 3D truncated spherical cavity
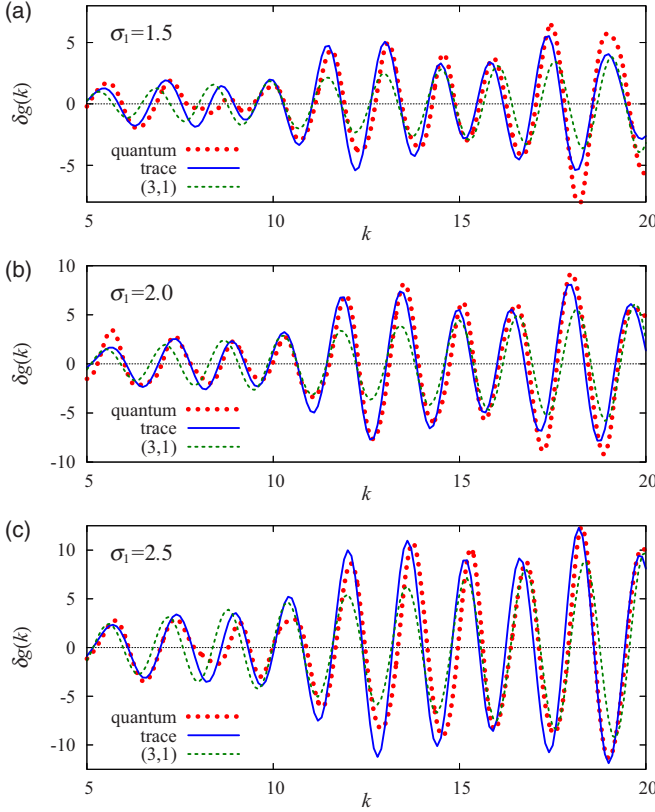
FIG. 17. Oscillating part of the level density with averaging width $\gamma = 0.3$ for several values of σ_1. The semiclassical trace formula, taking account of three shortest prefragment orbit families [solid (blue) line], is compared with the quantum level density [thick dotted (red) line]. The contribution of the triangle orbit families (3,1) [broken (green) line] is also shown.

systems. In addition to the truncated portion of the original families, contributions of the marginal orbits should be considered independently as the end-point correction to the former. In applications to the 2D billiard and 3D cavity potentials with TQS shape parametrization, my formulas successfully reproduce the quantum mechanical results. Although the contributions of the marginal orbits are expected to play minor roles in the semiclassical limit due to the lower degeneracies, it turns out that they play a significant role in the shell effects in the energy region of nuclei. Their effect is important especially for relatively small elongation where only a small portion of the parameter space is occupied by the fully degenerate periodic-orbit families, and it would be responsible for a prefragment shell effect emerging at a rather early stage of the fission deformation process.

Using my trace formula, the shell effect associated with the prefragments is extracted in a simple and natural way and can be evaluated quantitatively through the nuclear fission processes. The periodic orbit theory with the formula derived in this work would thus provide us a powerful tool to investigate the nuclear fission dynamics. Detailed analysis of the potential energy surface, taking into account the asymmetric shape degree of freedom in the TQS cavity model, and discussions

on the origin of asymmetric fission will be presented in a separate paper [25].

APPENDIX: TRACE FORMULA FOR MARGINAL ORBITS

1. Three-parameter family contribution

For a regular polygon orbit (p, t) in the three-dimensional spherical cavity potential, the generic formula (2.6) can be written as [4]

$$g_{pt}(E) = \frac{2M}{\hbar^2} \, \text{Re} \, \frac{\sin \varphi_{pt}}{\pi k R^{p-1}} \left(\frac{ik}{4\pi} \right)^p \int dS_1 \cdots dS_p e^{ikl_p}. \tag{A1}$$

In evaluating the surface integrals, the local surface coordinates (x_a, y_a) around the vertex P_a are defined as explained in Sec. II C (see Fig. 5).

For the three-parameter family of polygon orbits, the integrals over x_1, y_1, and y_2 should be exactly done, which gives the factor

$$\int dx_1 dy_1 dy_2 = 8\pi^2 R^3 \sin(2\varphi_{pt}) f_p \tag{A2}$$

with the occupation rate f_p given by Eq. (2.32). The other integrals are carried out using the SPA in the following way. The length of the orbit is expanded in $(2p - 3)$-dimensional surface coordinates $Ru = (x_2; x_3, y_3; \ldots; x_p, y_p)$ up to the quadratic order as

$$l(1, \ldots, p) = L_{pt} + \frac{R}{4} \sum_{ab} K_{ab} u_a u_b,$$

$$K_{ab} = \frac{2}{R} \frac{\partial^2 l_{pt}(u)}{\partial u_a \partial u_b}. \tag{A3}$$

L_{pt} is the length of the orbit (p, t). K represents the curvature matrix for the orbit, which is dimensionless, symmetric, and independent of the radius of the fragment. Using the SPA, the integrals are evaluated as

$$\int dx_2 dx_3 dy_3 \cdots dx_p dy_p e^{ikl(1 \cdots p)}$$

$$= R^{2p-3} e^{ikL_{pt}} \int d^{2p-3} u \, \exp \left[\frac{ikR}{4} \sum_{ab} K_{ab} u_a u_b \right]$$

$$= \frac{(4\pi i R/k)^{p-3/2}}{\sqrt{|\det K|}} e^{ikL_{pt} - i\pi n_-/2}, \tag{A4}$$

where n_- denotes the number of negative eigenvalues of K. Inserting (A2) and (A4) into Eq. (A1), one has

$$g_{pt}^{(\text{pr})}(E) = \frac{2MR^2}{\hbar^2} \frac{f_p \sin\varphi_{pt} \sin(2\varphi_{pt})\sqrt{kR}}{\sqrt{\pi |\det K|}}$$

$$\times \sin\left(kL_{pt} - \frac{\pi}{2}\mu_{pt}\right),$$

$$\mu_{pt} = 2p + n_- + \frac{1}{2}. \tag{A5}$$

The following relations have been checked numerically for each (p, t):

$$|\det K| = p \sin\varphi_{pt}, \quad 2p + n_- + \tfrac{1}{2} = 2t - p - \tfrac{3}{2} \,(\text{mod } 4) \tag{A6}$$

and $g_{pt}^{(\text{pr})}$ coincides with the Balian-Bloch formula $g_{pt}^{(\text{sph})}$ for $f_p = 1$ [see Eq. (2.14)]. Thus one has the contribution of the three-parameter family as

$$g_{pt}^{(\text{pr})}(E) = f_p g_{pt}^{(\text{sph})}(E)$$

$$= \frac{2MR^2}{\hbar^2} f_p \sqrt{kR} A_{pt}^{(\text{sph})} \sin\left(kL_{pt} - \frac{\pi}{2}\mu_{pt}\right), \tag{A7}$$

$$A_{pt}^{(\text{sph})} = \frac{\sin\varphi_{pt} \sin 2\varphi_{pt}}{\sqrt{\pi |\det K|}} = \sin 2\varphi_{pt}\sqrt{\frac{\sin\varphi_{pt}}{\pi p}}, \tag{A8}$$

$$\mu_{pt} = 2t - p - \frac{3}{2}, \tag{A9}$$

where A_{pt} represents the dimensionless amplitude which is independent of k and R.

2. Contribution of the marginal orbit families with one vertex on the joint

To evaluate the contribution of the marginal family to the integral (A1), any vertex can be put on the joint of the spherical surface and the neighboring surface, and each gives an identical contribution. Thus, one can put the first vertex on the joint and multiply it with p. The marginal orbits form a two-parameter family for polygon $(p > 2t)$ and a one-parameter family for diameter $(p = 2t)$. For a marginal polygon, the surface coordinates ξ_1 and y_2 should be exactly integrated. $\xi_1 = R\varphi_1 \sin\vartheta_A$ is related to the rotation about the symmetry axis $(0 \leqslant \varphi_1 \leqslant 2\pi)$, and $y_2 = R\psi \sin(2\varphi_{pt})$ to the rotation about the axis OP_1 with angle ψ over the range $4\psi_p$. The integrations over these variables give the factor

$$\int d\xi_1 dy_2 = 8\pi R^2 \psi_p(\vartheta_A) \sin\vartheta_A \sin(2\varphi_{pt}). \tag{A10}$$

Integrating over the rest of $2p - 2$ variables $R\boldsymbol{u} = (\eta_1; x_2, x_3, y_3; \ldots; x_p, y_p)$ using the SPA by expanding the length l_p as (A3), one has

$$\int dS_1 \cdots dS_p e^{ikl(1\cdots p)}$$

$$= p \times \frac{1}{2} \times 8\pi R^{2p} \psi_p(\vartheta_A) \sin\vartheta_A \sin(2\varphi_{pt})$$

$$\times e^{ikL_{pt}} \int d^{2p-2}u \, \exp\left[\frac{ikR}{4}\sum_{ab} K'_{ab}u_a u_b\right]$$

$$= \frac{4\pi p R^{2p} \psi_p(\vartheta_A) \sin\vartheta_A \sin(2\varphi_{pt})(4\pi i)^{p-1}}{(kR)^{p-1}\sqrt{|\det K'|}}$$

$$\times e^{ikL_{pt} - i\frac{\pi}{2}n'_-}. \tag{A11}$$

In the middle expression, the factor p appears because any of the p vertices can be put on the joint as stated above. The next factor $1/2$ is to compensate foe the integration range of η_1, which is actually $\eta_1 > 0$ but extended to $(-\infty < \eta_1 < \infty)$ by assuming that the surface around the vertex P_1 is the extension of the neighboring wall outside the spherical surface. n'_- counts the number of negative eigenvalues of the $(2p - 2)$-dimensional curvature matrix K'. In consequence, one obtains

$$g_{pt}^{(\text{mg})}(E) = \frac{2MR^2}{\hbar^2} A_{pt}^{(\text{mg})} \sin\left(kL_{pt} - \frac{\pi}{2}\mu_{pt}^{(\text{mg})}\right), \tag{A12}$$

with

$$A_{pt}^{(\text{mg})} = \frac{p\psi_p(\vartheta_A) \sin\varphi_{pt} \sin(2\varphi_{pt}) \sin\vartheta_A}{\pi\sqrt{|\det K'|}} \tag{A13}$$

$$\mu_{pt}^{(\text{mg})} = 2p + n'_-. \tag{A14}$$

The above equations are valid for a primitive polygon family. For a repeated polygon $m(p, t)$, the $j(p + 1)$th vertex $(1 \leqslant j < m)$ on the joint can be placed either on the spherical surface or on the neighboring surface. Therefore, one should sum over all 2^{m-1} combinations (labeled β) for the choice of the surfaces:

$$g_{m(p,t)}^{(\text{mg})}(E) = \frac{2MR^2}{\hbar^2} \sum_{\beta} A_{m(p,t),\beta}^{(\text{mg})} \sin\left(kmL_{pt} - \frac{\pi}{2}\mu_{m(p,t),\beta}^{(\text{mg})}\right), \tag{A15}$$

with

$$A_{m(p,t),\beta}^{(\text{mg})} = \frac{p\psi_p \sin\varphi_{pt} \sin(2\varphi_{pt}) \sin\vartheta_A}{2^{m-1}\pi\sqrt{|\det K'_\beta|}}, \tag{A16}$$

$$\mu_{m(p,t),\beta}^{(\text{mg})} = 2mp + n'_\beta. \tag{A17}$$

The marginal diameter orbits $(2t, t) = t(2, 1)$ form a one-parameter family generated by the rotation about the symmetry axis. Their contribution to the level density is derived in the same way as above, and one has

$$g_{t(2,1)}^{(\text{mg})}(E) = \frac{2MR^2}{\hbar^2} \sum_{\beta} \frac{A_{t(2,1),\beta}^{(\text{mg})}}{\sqrt{kR}} \sin\left(ktL_2 - \frac{\pi}{2}\mu_{t(2,1),\beta}^{(\text{mg})}\right), \tag{A18}$$

with

$$A_{t(2,1),\beta}^{(\text{mg})} = \frac{\sin\vartheta_A}{2^{t-1}\sqrt{\pi |\det K'_\beta|}}, \tag{A19}$$

$$\mu_{t(2,1),\beta}^{(\text{mg})} = n'_\beta - \frac{1}{2}. \tag{A20}$$

3. Marginal polygon family with two vertices on the joint

For a polygon orbit family, there is the possibility of two vertices being placed on the joint. This forms a one-parameter family according to the rotation about the symmetry axis. The integration with respect to $x_1 = R\varphi_1 \sin\vartheta_A$ gives the factor $2\pi R \sin\vartheta_A$, and other $2p-1$ integrals are carried out by using the SPA. The curvature K'' is calculated under the assumption that the two vertices are on the neighboring surface. Taking account of the $2p$ possible ways of selecting the two vertices on the joint, and the extensions of surface integration ranges for the two surface coordinates from $(0, \infty)$ to $(-\infty, \infty)$, one has

$$\int dS_1 \cdots dS_p e^{ikl(1\cdots p)}$$
$$= 2p \times \frac{1}{4} \times 2\pi R^{2p} \sin\vartheta_A \frac{(4\pi i/kR)^{p-1/2}}{\sqrt{|\det K''|}} e^{ikL_{pt} - i\pi n''_-/2}. \tag{A21}$$

Thus, the contribution to the level density is given by

$$g_{pt}^{(\mathrm{mm})}(E) = \frac{2MR^2}{\hbar^2} \frac{A_{pt}^{(\mathrm{mm})}}{\sqrt{kR}} \sin\left(kL_{pt} - \frac{\pi}{2}\mu_{pt}^{(\mathrm{mm})}\right), \tag{A22}$$

$$A_{pt}^{(\mathrm{mm})} = \frac{p \sin\varphi \sin\vartheta_A}{2\sqrt{\pi|\det K''|}}, \tag{A23}$$

$$\mu_{pt}^{(\mathrm{mm})} = 2p + n''_- - \frac{1}{2} \tag{A24}$$

for a primitive orbit family. In cases of repeated orbits, one has to consider all the possible combinations of the surfaces for intermediate reflections on the joint as in Eq. (A15).

4. Total contribution of the fragment-orbit family

Summarizing the above contributions, the total contribution of the orbit family (p, t) confined in the spherical fragment is given by

$$g_{pt}^{(\mathrm{frag})}(E) = \frac{2MR^2}{\hbar^2} \sum_{D=1}^{3} (kR)^{\frac{D-2}{2}} A_{pt}^{(D)} \sin\left(kL_{pt} - \frac{\pi}{2}\mu_{pt}^{(D)}\right), \tag{A25}$$

where the summation over principal and marginal terms is expressed as the sum over the degeneracy D. The amplitudes and Maslov indices are given by

$$A_{pt}^{(3)} = f_p A_{pt}^{(\mathrm{sph})}, \quad \mu_{pt}^{(3)} = \mu_{pt},$$
$$A_{pt}^{(2)} = A_{pt}^{(\mathrm{mg})}, \quad \mu_{pt}^{(2)} = \mu_{pt}^{(\mathrm{mg})},$$
$$A_{pt}^{(1)} = A_{pt}^{(\mathrm{mm})}, \quad \mu_{pt}^{(1)} = \mu_{pt}^{(\mathrm{mm})} \tag{A26}$$

for a polygon ($p > 2t$), and

$$A_{2t,t}^{(3)} = 0,$$
$$A_{2t,t}^{(2)} = f_2 A_{2t,t}^{(\mathrm{sph})}, \quad \mu_{2t,t}^{(2)} = \mu_{2t,t}^{(\mathrm{sph})},$$
$$A_{2t,t}^{(1)} = A_{2t,t}^{(\mathrm{mm})}, \quad \mu_{2t,t}^{(1)} = \mu_{2t,t}^{(\mathrm{mm})} \tag{A27}$$

for a diameter. The level density in terms of the wave-number variable k is expressed as

$$g_{pt}^{(\mathrm{frag})}(k) = \frac{\hbar^2 k}{M} g_{pt}^{(\mathrm{frag})}(E)$$

$$= 2R \sum_{D=1}^{3} (kR)^{D/2} A_{pt}^{(D)} \sin\left(kL_{pt} - \frac{\pi}{2}\mu_{pt}^{(D)}\right) \tag{A28}$$

$$= 2R \operatorname{Im}\left[\left\{\sum_D (kR)^{D/2} A_{pt}^{(D)} e^{-i\pi\mu_{pt}^{(D)}/2}\right\} e^{ikL_{pt}}\right]$$

$$\equiv 2R \operatorname{Im}[\mathcal{A}_{pt}(kR) e^{ikL_{pt}}]. \tag{A29}$$

[1] M. C. Gutzwiller, J. Math. Phys. **12**, 343 (1971).
[2] M. C. Gutzwiller, *Chaos in Classical and Quantum Mechanics* (Springer-Verlag, New York, 1990).
[3] R. Balian and C. Bloch, Ann. Phys. (N.Y.) **63**, 592 (1971).
[4] R. Balian and C. Bloch, Ann. Phys. (N.Y.) **69**, 76 (1972).
[5] A. Bohr and B. R. Mottelson, *Nuclear Structure, Vol. II* (Benjamin, Reading, 1975).
[6] V. M. Strutinsky and A. G. Magner, Sov. J. Part. Nucl. **7**, 138 (1976).
[7] V. M. Strutinsky, A. G. Magner, S. R. Ofengenden, and T. Døssing, Z. Phys. A **283**, 269 (1977)
[8] H. Nishioka, K. Hansen, and B. R. Mottelson, Phys. Rev. B **42**, 9377 (1990).
[9] M. Brack, J. Damgaard, A. S. Jensen, H. C. Pauli, V. M. Strutinsky, and C. Y. Wong, Rev. Mod. Phys. **44**, 320 (1972).
[10] K. Arita, A. Sugita, and K. Matsuyanagi, Prog. Theor. Phys. **100**, 1223 (1998).
[11] A. G. Magner, K. Arita, S. N. Fedotkin, and K. Matsuyanagi, Prog. Theor. Phys. **108**, 853 (2002).
[12] A. G. Magner, I. S. Yatsyshyn, K. Arita, and M. Brack, Phys. At. Nucl. **74**, 1445 (2011).
[13] M. Brack, S. M. Reimann, and M. Sieber, Phys. Rev. Lett. **79**, 1817 (1997).
[14] A. N. Andreyev *et al.*, Phys. Rev. Lett. **105**, 252502 (2010).
[15] T. Ichikawa, A. Iwamoto, P. Möller, and A. J. Sierk, Phys. Rev. C **86**, 024610 (2012).
[16] U. Mosel and H. W. Schmitt, Nucl. Phys. A **165**, 73 (1971).
[17] M. Warda, A. Staszczak, and W. Nazarewicz, Phys. Rev. C **86**, 024601 (2012).
[18] J. D. McDonnell, W. Nazarewicz, and J. A. Sheikh, Phys. Rev. C **87**, 054327 (2013).
[19] See e.g., R. Courant and D. Hilbert, *Methods of Mathematical Physics, Vol. II* (Wiley, New York, 1989).
[20] S. C. Creagh and R. G. Littlejohn, Phys. Rev. A **44**, 836 (1991).
[21] S. C. Creagh and R. G. Littlejohn, J. Phys. A: Math. Gen. **25**, 1643 (1992).
[22] S. M. Reimann, M. Brack, A. G. Magner, J. Blaschke, and M. V. N. Murthy, Phys. Rev. A **53**, 39 (1996).
[23] M. Brack and R. K. Bahduri, *Semiclassical Physics* (Westview, Boulder, 1996).
[24] J. R. Nix, Nucl. Phys. A **130**, 241 (1969).
[25] K. Arita, T. Ichikawa, and K. Matsuyanagi, Phys. Rev. C **98**, 064311 (2018).